manuscript accepted by *Water Resources Research*

Quantifying the effects of bed roughness on transit time distributions via direct numerical simulations of turbulent hyporheic exchange

Guangchen Shen[1], Junlin Yuan[1], and Mantha S. Phanikumar[2]

[1]Department of Mechanical Engineering, Michigan State University, East Lansing, MI 48824, USA
[2]Department of Civil and Environmental Engineering, Michigan State University, East Lansing, MI 48824, USA

Key Points:

- Transit times calculated with particle tracking using pore-resolved velocities from DNS of turbulent surface-subsurface flows
- DNS enables direct evaluation and comparison of various mechanisms contributing to hyporheic exchange
- Roughness texture modifies transit time values but not heavy-tail slope of transit time distribution

Corresponding author: Junlin Yuan, junlin@msu.edu

Abstract

We report direct numerical simulation (DNS) results of hyporheic exchange for a macroscopically flat river bed with two different particle roughness textures, at a surface flow friction Reynolds number $Re_\tau = 395$ and a bed permeability Reynolds number $Re_K = 2.6$. Transit time distributions, subsurface flow patterns and the interfacial volumetric fluxes are discussed. The transit time was quantified using a forward particle tracking method based on pure advection by three-dimensional, pore-resolved, time-mean velocities. Results show that bed roughness induces deep subsurface flow paths that yield a transit time distribution with a power-law tail. Roughness obstructs the surface flow, creating interfacial pressure variations which induce subsurface flow. Next, the molecular diffusion is accounted for based on a random walk method and is shown to increase transit times regardless of roughness texture. This work demonstrates that particle roughness on a macroscopically flat sediment bed can induce significant hyporheic exchange that is fundamentally similar to that induced by bedforms.

Plain Language Summary

Riverine flows are turbulent flows with wide range of scales of motion in both space and time. Driven and modified by natural and anthropogenic factors, channel flows interact with local features (e.g., bars, ripples and dunes) and smaller features down to the scale of individual sediment grains. The magnitude of exchange of water with bed sediment (hyporheic exchange) and the time water molecules spend within the bed before reentering the channel are key details that control water quality in streams, as they determine the nature of biogeochemical processes. The role played by processes at the scale of individual grains and grain clusters (collectively referred to as bed roughness) have not been understood. We use direct simulation of turbulent flows and consider two "flat bed" scenarios with regular or random roughness at the sediment-water interface. We show that bed roughness induces deep flow paths and long transit times similar to those produced by local features and that the roughness texture plays an important role. The results offer novel insights into small-scale hyporheic flows and provide quantitative estimates of the inherent uncertainty that can be expected in estimates of hyporheic exchange due to changes at larger scales.

1 Introduction

The hyporheic zone, the region in and around a stream channel where ground water and stream water mix, plays an important role in biogeochemical processes in stream ecosystems (Boano et al., 2014). Hyporheic mixing (Shen et al., 2020; Roche et al., 2019) near sediment-water interfaces is controlled by several factors including the hydraulic gradient and the mean grain size (Malard et al., 2002) and directly influences the fluxes of water and solutes (nutrients, dissolved organic carbon and oxygen) by transferring momentum and energy across the interface. In addition to exchange fluxes, the role of hyporheic zones in transforming the chemical signature of stream water depends, among other factors, on transport time scales often described using transit time distributions (TTDs) and residence time distributions (RTDs). For a solute mass pulse entering the river bed at time t, the residence time τ is the age of a water parcel in the bed (Elliott & Brooks, 1997b). Transit time, on the other hand, is the residence time or water age at the time a parcel of water exits the system and therefore represents the maximum residence time (or age) that can be attained by a water parcel for a given flow path. RTDs and TTDs are related and they have both been extensively used in hyporheic zone research. For example, residence times have been used to evaluate the ability of the hyporheic zone to process nutrients (Boano et al., 2014) and to classify hyporheic zones (Harvey, Böhlke, et al., 2013). Transit times have been used to understand the kinematics of age mixing processes in advection-dispersion models (Benettin et al., 2013) as well as rela-

tions between flow, storage and chloride transport in a small watershed (Benettin et al., 2015; Harman, 2015), to infer changes in water cycle dynamics in managed landscapes (Danesh-Yazdi et al., 2016) and to understand biogeochemical reactions in a dam-regulated river corridor (Song et al., 2020). Median transit times have been used to assess the reaction efficiency of hyporheic flows by defining a Damköhler number representing the ratio of transport and biogeochemical time scales (Song et al., 2020).

Bed geometry and morphology exert a strong influence on exchange fluxes and transit times. Bed geometries are often multiscale, with both large- and small-scale features contributing to the exchange (Aubeneau et al., 2015; Persson et al., 2005; Stubbs et al., 2018; Lee et al., 2020; Worman et al., 2006). For example, large-scale features such as bars that scale with bankfull depth and channel width, relatively small-scale features such as bedforms, as well as roughness details at the scale of individual grains all influence exchange fluxes. Existing studies on flow and residence/transit times are typically focused on the effects of morphological features such as ripples and dunes that are orders of magnitude larger than individual sediment grains. Elliott and Brooks (1997b) (henceforth referred to as EB97) analytically solved for the velocity field and residence time for an ideal subsurface flow model with a sinusoidal bedform. The solutions were based on a two-dimensional (2D) Darcy equation with prescribed pressure distribution at the bed surface; these solutions described the "pumping" mechanism of the exchange, induced by pressure variations along the bed surface as a result of local flow acceleration and deceleration. The time a fluid particle spends along its subsurface flow path was calculated using a numerical particle tracking approach. The model of EB97 considered only advection (by the spatially and temporally averaged Darcy velocity) for flow path tracking, while in Elliott (1991) additional mixing mechanisms (turbulent mixing or molecular diffusion of solutes) were also accounted for by using a random walk method. In the above methods, a constant solute concentration is assumed in the fluid column; in other words, the flow is assumed well mixed.

Examples of the application of the Darcy model for subsurface flow calculation and particle tracking to estimate residence time based on advective exchange (EB97) include the following, among many others. Packman et al. (2000) applied a model of pumping exchange to colloid transport and filtration. They calculated the residence time by superimposing advective transport and particle settling in the bed and included the effect of physicochemical filtration by bed sediment also. Wörman et al. (2002) developed a framework to integrate the residence time estimation based on the method of Packman et al. (2000) with a model of longitudinal solute transport in streams. Many studies, such as Salehin et al. (2004) and Laube et al. (2018), characterized hyporheic exchange within heterogeneous streambeds. It was shown that, in a heterogeneous bed compared to a homogeneous one, the shorter and faster preferential hyporheic flow paths lead to more rapid net hyporheic exchange and a smaller hyporheic zone. Laube et al. (2018) further developed a modeling strategy for an equivalent conductivity tensor. Several recent studies incorporated pore-scale simulation results into the particle tracking model (Sun et al., 2015; Kim & Kang, 2020). Kim and Kang (2020) studied the 2D pore-scale transport phenomena across a surface-subsurface interface, with the turbulence modeled using a Reynolds-averaged Navier-Stokes (RANS) closure.

Most of the studies summarized above quantified residence time using conceptual models of bedform features (such as ripples or dunes). Detailed aspects of solute transport near the bed, including turbulent mixing and pore-scale dynamics, are rarely studied. At the "micro" scale of pore flow, the hydrodynamic effects of bed roughness formed by the uppermost-layer of sediment grains and their arrangement are likely to be important, as the benthic biolayer where important nutrient or pollutant processing occurs is limited to a thin layer (of 2-5 cm) beneath the streambed surface (Battin et al., 2008; Harvey, Bohlke, et al., 2013; Knapp et al., 2017). In addition, in a warmer climate streambed roughness is expected to increase as a result of enhanced bioturbation—the effect of small

animals, such as chironomid larvae and tubificid worms, within the sediment bed as they rework the sediment (Baranov et al., 2016; Dairain et al., 2020).

The effects of wall roughness on turbulence were predominantly studied for flows over impermeable walls (see reviews by Jiménez (2004) and Flack and Schultz (2014)). Typically, roughness is categorized as bed height variations in the range between $5\delta_\nu$ and 0.1δ (where $\delta_\nu = \nu/u_\tau$ is the viscous length scale, ν is the kinematic viscosity of the fluid, u_τ is the friction velocity, and δ is the turbulent boundary layer thickness, or the channel depth in the present half channel simulations). Roughness affects turbulence by increasing wall friction and enhancing turbulence production near the wall. In the context of turbulent flow bounded by a permeable wall (such as the region near a sediment-water interface), bed roughness likely affects the flow near the bed and consequently the mass exchange also.

Some insights into how small-scale features of bed topography (e.g., grain-scale irregularities) may affect the exchange were provided by a few studies on multiscale or fractal bed topographies. Aubeneau et al. (2015) performed laboratory measurements of solute transport with sand beds for different discharges. They found that fractal properties of the bed topography affect solute residence time distributions. The larger bedforms induced more hyporheic exchange but shorter residence times, as shown by the steeper slope of the washout breakthrough curve. Lee et al. (2020) analyzed the effect of fractal properties of the bed topography on interfacial flux and residence time, based on coupled RANS of channel flow and subsurface flow calculated using a Darcy model. Residence times were calculated using the random walk particle tracking method. They observed that the interfacial flux increases with the fractal dimension of the bed (i.e., prominence of smaller topographical features or scales).

Recent pore-resolved direct numerical simulations (DNS) of interface turbulence carried out by the authors (Shen et al., 2020) revealed that, even in the absence of bedforms, the grain-scale roughness of a macroscopically flat bed leads to significant fluid volumetric flux into the sediment. Also, statistics and structure of the turbulent flow were shown to depend on the texture of roughness. Similar observations were made for a macroscopically flat bed by Chandler et al. (2016), Grant et al. (2019) and Kim and Kang (2020). In this paper, we expand the work by Shen et al. (2020) by documenting the effects of grain-scale roughness and its texture on macroscopic exchange quantities including the fluid volumetric flux into the sediment, subsurface flow paths, and transit time characteristics. The primary questions that will be addressed in this research include: (1) How does bed roughness on a macroscopically flat bed influence fluid parcel transit times? (2) How do TTDs change with tracer particle entry/exit locations within a three-dimensional flow field and with the inclusion of molecular diffusion? To this end, turbulent open-channel flows bounded by synthesized sediment beds similar to those studied by Shen et al. (2020) were simulated. Computed flows for two sediment beds that share the same bed permeabilities but have different bed roughness arrangements are compared. A forward particle tracking method is used to calculate the transit times, considering the mechanism of time-mean velocity advection with and without molecular diffusion. The paper is organized as follows. Section 2 describes the details of the DNS simulations, the sediment bed synthesis, and the method used to calculate transit times. Section 3 compares the transit time results for the two cases examined and analyzes the effects of molecular diffusion, followed by conclusions in Section 4.

2 Methodology

2.1 Governing equations

The governing equations of the DNS simulations of water flow are summarized below. The incompressible flow of a Newtonian fluid is governed by the equations of con-

servation of mass and momentum:

$$\frac{\partial u_i}{\partial x_i} = 0, \tag{1}$$

$$\frac{\partial u_j}{\partial t} + \frac{\partial u_i u_j}{\partial x_i} = -\frac{\partial P}{\partial x_j} + \nu \nabla^2 u_j + F_j. \tag{2}$$

Here, x_1, x_2 and x_3 (or x, y and z) are, respectively, the streamwise, bed-normal and spanwise directions, and u_j (or u, v and w) are the velocity components in those directions; $P = p/\rho$ is the modified pressure, where p is the static pressure and ρ is the density. A Cartesian mesh is used. The term F_j in Equation (2) represents a body force prescribed by an immersed boundary (IB) method to impose no-slip boundary conditions on the fluid-solid interface. The sediment grain geometry is well-resolved by the grid; a grain is resolved by 50 grid points in each direction. The IB method employed here is based on the volume-of-fluid approach (Scotti, 2006); its detailed implementation and validation are provided by Yuan and co-workers (Yuan & Piomelli, 2014a, 2014b; Yuan et al., 2019). The F_i values are negligible except in the cells that are cut by the immersed solid boundaries. The simulations are performed using a code that was validated extensively for a variety of turbulent flows in the past for different types of turbulent flows (Keating et al., 2004; Piomelli & Yuan, 2013; Wu et al., 2019; Mangavelli et al., 2021; Shen et al., 2020). The code solves the governing equations (1) and (2) on a staggered grid using second-order, central differences for all terms, with semi-implicit time advancement (second-order Adams-Bashforth scheme for the bed-normal diffusion term) and MPI parallelization.

Fully developed open-channel flows are simulated. The simulation domain includes both the surface and sub-surface flows (Figure 1(a,b)). δ is the thickness of the turbulent boundary layer (i.e., open-channel height) measured from the sediment crest; H_s is the sediment depth measured from the crest to the bottom boundary of the simulation domain. Symmetric boundary conditions are applied at both top and bottom boundaries of the domain. Periodic conditions are applied at x and z boundaries. A constant mean pressure gradient is used to drive the flow. The elevation of $y = 0$ is set at the virtual origin—an offset of the y axis such that the mean velocity profile in the overlap region of the turbulent flow recovers its logarithmic form. The elevation of the virtual origin was determined based on a fitting procedure (Breugem et al., 2006; Manes et al., 2011); it falls between $0.3D$ and $0.5D$ below the sediment crest, where D is the grain diameter.

In the sediment, the presence of grains leads to spatial heterogeneity of time-averaged variables. These time-averaged fluctuations are separated from turbulent fluctuations using the double-averaging (DA) decomposition introduced by Raupach and Shaw (1982),

$$\phi(x_i, t) = \langle \overline{\phi} \rangle(y) + \widetilde{\phi}(x_i) + \phi'(x_i, t) \tag{3}$$

where ϕ is an instantaneous flow variable, $\langle \phi \rangle$ is the intrinsic spatial average in the (x, z)-plane, $\langle \phi \rangle = 1/A_f \int_{A_f} \phi dA$ (where A_f is the area occupied by fluid), $\overline{\phi}$ is the temporal average, $\phi' = \phi - \overline{\phi}$ is the instantaneous turbulent fluctuation, and $\widetilde{\phi} = \overline{\phi} - \langle \overline{\phi} \rangle$ is called the form-induced (or dispersive) fluctuation.

2.2 Case configuration and parameters

The simulation parameters are listed in Table 1. Two cases are considered, one with a regular interface (Case 1) in which the arrangement of grains in the uppermost layer is regular and the other with random arrangement of grains (termed 'random interface', Case 2). In both cases, the same porosity of 0.41 is imposed in the sediment sufficiently far from the interface. The permeability Reynolds number and the friction Reynolds number are the same for both cases: $Re_K = \sqrt{K} u_\tau / \nu = 2.62$ (where K is the permeability) and $Re_\tau = \delta u_\tau / \nu = 395$. Following Voermans et al. (2017), u_τ is obtained from

Table 1. Summary of simulation parameters.

	Interface	Re_K	Re_τ	D/δ	D^+	H_s/δ	$(L_x, L_z)/\delta$	$(\Delta x^+, \Delta y^+_{\min}, \Delta z^+)$
Case 1	Regular	2.62	395	0.20	79	1.6	$(6, 3)$	$(1.5, 0.19, 1.5)$
Case 2	Random	2.62	395	0.20	79	1.6	$(6, 3)$	$(1.5, 0.19, 1.5)$

Note. D is the grain diameter; L_{x_i} is the simulation domain size in x_i. Δx^+, Δy^+, and Δz^+ are DNS grid sizes in x, y and z, respectively, normalized using the viscous length scale ν/u_τ.

the maximum magnitude of the bed-normal profile of the total shear stress, which is the sum of the viscous shear stress, the Reynolds shear stress and the form-induced shear stress. The total numbers of grid points are 1536, 779 and 768 in x, y and z directions, respectively. The present DNS simulations are similar to the simulations reported by Shen et al. (2020). The only difference is that the sediment thickness herein is doubled ($H_s/\delta = 1.6$ versus 0.8 in Shen et al. (2020)), to allow for deeper subsurface flow paths, which are important for calculation of large transit times but less important for interfacial turbulence. The total simulation time used for data collection is around 10 large-eddy turnover times (LETOTs), defined as δ/u_τ; a LETOT represents the time scale of the evolution of the largest turbulent eddy in the open channel. Sufficiency of the data sampling in time was validated by comparing both surface and subsurface flow statistics, as well as TTDs, obtained with 10 LETOTs and those obtained with 20 LETOTs. The differences were small (e.g., up to 1% in subsurface dispersive velocities, $\langle \widetilde{u}^2 \rangle^{1/2}$, as shown in the Supporting Information Figure S4).

For both cases, the depths of the channel and the bed (both measured from the virtual origin) are 5 times and 8 times of the grain diameter, respectively. A boundary layer thickness of 5 times the grain size is much smaller than in many streams in reality and, consequently, the turbulence near the interface may not be identical to those in many real streams. However, the present setup is designed to represent streams for the regime with Re_K of $o(1)$ where the form-induced velocity is the main component of the subsurface fluid motion; the interfacial turbulence weakly affects the majority of the parcel transit times in comparison to the form-induced velocities. In addition, D/δ of the same order of magnitude were used in existing numerical and experimental studies that reported grain-scale physics (Manes et al., 2009; Dey & Das, 2012; Fang et al., 2018; Han et al., 2018; Voermans et al., 2017, 2018).

The porous sediment beds are modeled as closely packed monodisperse hard spheres. In the bulk of the sediment, the sphere positioning is determined based on molecular dynamics simulations (Plimpton, 1995) and is random for both cases. For the uppermost-layer spheres, two types of distributions are imposed, representing regular (Case 1) and random (Case 2) bed roughness geometries, respectively. The random case corresponds to significantly larger root-mean-square roughness height and longer horizontal correlation lengths. As these length scales are much smaller compared to δ and the scales typical of a bedform, the bed height variation is considered as roughness. Figures 1(a,b) compare the sphere distributions in Cases 1 and 2, showing the difference in grain arrangement at the top of the sediments. The sediment in Case 2 was constructed such that it yields turbulence statistics that match those observed for randomly poured spheres in the experimental studies of Voermans et al. (2017) (case L12 therein). Case 2 is thus considered as a good approximation of a realistic sediment.

To highlight the difference between the two roughness geometries, the one-dimensional (1D) power spectra of height fluctuations of uppermost-layer spheres (E_k) are compared in Figure 1(c) as functions of the streamwise wavenumber ($\kappa_1 = 1/\lambda_1$, where λ_1 is the streamwise wavelength). Both cases show a white noise regime at small wavenumbers,

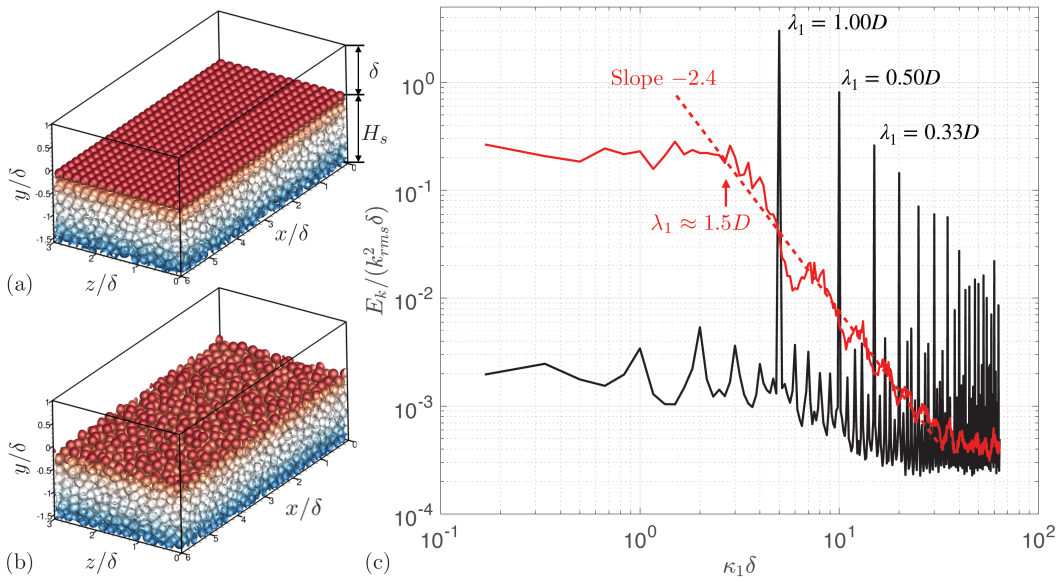

Figure 1. Simulation domain and synthesized sediment beds colored by y in (a) the regular and (b) the random cases. (c) One-dimensional power spectral densities E_k of the interface height fluctuations for Case 1 (regular case, ———) and Case 2 (random case, ———). - - - Slope of power-law decay for Case 2; k_{rms} is the root-mean-square (rms) of interface height fluctuations.

characterized by almost constant E_k. Aubeneau et al. (2015) calculated the power spectra of elevations of sand beds produced in lab flume experiments under various discharges. They also observed a white noise region in the power spectrum for small wavenumbers. For the random case the white noise regime applies to λ_1/D larger than around 1.5. For smaller λ_1, E_k shows a power-law decay with a slope of around -2.4. From this power-law decay, a fractal dimension D_f can be identified as $D_f = E + (3 - \beta)/2 = 2.3$, where $\beta = 2.4$ is the fitted slope of the decay and $E = 2$ (for a 3D surface) is the Euclidean topological dimension. Aubeneau et al. (2015) also observed power-law decays at large wavenumbers, though with different slopes of -1.0 to -1.5. In comparison, for the regular case the white noise region covers wavenumbers up to D. At larger wavenumbers E_k is characterized by higher-frequency harmonics, which is a mathematical consequence of the slight clipping (or flattening) at the top of the sphere surfaces that results from the spatial discretization of the sphere geometry. These observations show that the bed roughness of Case 2 is close to a self-affine fractal (similar to real sediment beds) while Case 1 is characterized by organized grain-wise protuberances.

2.3 Transit time calculation based on particle tracking

For an unsteady flow in general, the mass conservation equation for the storage of water of a certain age in the sediment is (Botter et al., 2011; Harman, 2015)

$$\frac{\partial S(t) p_S(\tau,t)}{\partial t} = -Q(t)\overleftarrow{p}_Q(\tau,t) - \frac{\partial S(t) p_S(\tau,t)}{\partial \tau}, \tag{4}$$

where $S(t)$ is the instantaneous total water storage in the sediment at time t, $Q(t)$ is the instantaneous flux at the outflow, $p_S(\tau,t)$ is the instantaneous RTD, defined as the probability density function (pdf) of the age (τ) of all the water parcels in the sediment at time t, and $\overleftarrow{p}_Q(\tau,t)$ is the backward TTD, defined as the probability that the age of a water parcel at the outflow at time t is equal to τ (Harman, 2015). The only assump-

tion used in Equation (4) is that there is one inlet and one outlet of the system. In this study, the inlet is the collection of regions on the water-sediment interface where the bed-normal velocity (v) is negative, while the collection of regions where v is positive serves as the outlet. The water age is considered zero at the inlet.

Note that different definitions of RTD were used in the literature. For example, the cumulative distribution function of RTD was defined as the fraction of solute entering the sediment bed in a short time near $t = 0$ and exiting the bed by time τ (Grant et al., 2020). The residence time function of EB97 is the complement of this definition. In this article, however, the definitions of Harman (2015) are followed.

We consider fluid parcels advected by the three-dimensional, time-averaged velocity, $\overline{u}_i$. The advection by instantaneous turbulent fluctuations u_i' is not accounted for. This is because, at the present $Re_K = 2.6$, the magnitudes of normal Reynolds stress components are significantly smaller than those of the form-induced stresses in the sediment below the Brinkman layer, as shown by the DNS data of Shen et al. (2020) for the present cases. At a higher Re_K range, however, the effect of u_i' on the transit times is likely to be more important inside the sediment (Voermans et al., 2017). Kim et al. (2020) showed that at $Re_K = 50$ and $Re_\tau \approx 2,000$ significant turbulent motions in the bed—including downwelling and upwelling flows—occur and are modulated by large-scale turbulent motions in the surface flow. The present analyses, therefore, are relevant for the regime of $Re_K = o(1)$ only, where the interfacial turbulence is present but weak compared to dispersive velocities.

The consideration of the water parcels advected by the time mean velocity implies a steady state assumption for Equation (4), which becomes

$$Q\overleftarrow{\overline{p}}_Q(\tau) + S\frac{\partial p_S(\tau)}{\partial \tau} = 0. \tag{5}$$

Equation (5) shows that the backward TTD and the RTD are related; one can be calculated from the other given known values of the outflow flux and water storage. In this work, we calculate $\overleftarrow{\overline{p}}_Q(\tau)$ based on its definition. The discussion is focused on $\overleftarrow{\overline{p}}_Q(\tau)$ and the corresponding cumulative distribution function, $\overleftarrow{\overline{P}}_Q(\tau)$. The RTD can be calculated based on Equation 5; details are presented in the Supporting Information Section S1.

In the present particle tracking approach, a fluid parcel is considered as a tracked particle. To calculate the transit time (or the maximum water age achieved by an individual parcel in the sediment), fluid parcels are traced starting from a y elevation near the interface throughout the (x, z) plane. Only the fluid parcels entering the sediment (i.e., those released at locations where $\overline{v} < 0$) are tracked. The tracked paths are in general three-dimensional. The parcel position $x_i(t)$ at a time t (with $t = 0$ at the parcel release time) is tracked based on

$$\frac{dx_i}{dt} = \overline{u}_i[x_i(t)], \tag{6}$$

where t is a fictitious time used for particle tracking, not to be confused with the simulation time in DNS. Equation (6) is discretized and solved using the explicit Euler scheme. Once a subsurface travel path is determined, the transit time for the corresponding fluid parcel is calculated as the total time it spends along the subsurface path.

All tracked fluid parcels share the same release elevation (y_1) and the same 'exit' elevation (y_2). If $y_1 \leq y_2$, a parcel is considered to have left the sediment once it passes y_2. If $y_1 > y_2$, the tracked parcel first goes downward, passing the y_2 elevation, and then upward toward the y_2 elevation; in this case, the exit is considered to occur when the parcel passes y_2 the second time. The periodic boundary conditions in x and z are used: parcels leaving the domain at boundary $x/\delta = 6$ reenters the domain at boundary $x/\delta = 0$, and vice versa, for up to twice of the domain lengths. Longer tracking lengths up to

4 times of the domain lengths in x and z were also tested, yielding similar transit time distributions. One particle is released at each computational grid point in the fluid domain at $y = y_1$. In total, around $o(10^6)$ particles are released. To test the result convergence, we used twice the number of released particles, which led to differences of less than 1% in the fitted TTD slope and the median transit time value. The cumulative backward TTD, $\overleftarrow{P}_Q(\tau)$, is calculated as the fraction of the number of tracked subsurface paths that correspond to transit times shorter than τ. $\overleftarrow{p}_Q(\tau)$ is then obtained as $d\overleftarrow{P}_Q/d\tau$. The calculated $\overleftarrow{p}_Q(\tau)$ is smoothed based on a moving averaging procedure. The size of the averaging window widens with the transit time value as approximately 0.1τ.

To validate the implementation of the particle tracking method, the computed residence time function as defined in EB97 is compared to the analytical solution for a subsurface flow induced by a 2D sinusoidal interface pressure distribution. Details of the validation are included in the Supporting Information Section S2. The comparison shows that the particle-tracked residence time function matches well with the analytical solution given a sufficiently fine spatial resolution and a sufficiently deep sediment domain (Figure S2).

In the analyses of EB97, detailed flow information around sediment grains is not available. The water column and the subsurface flow were delineated by a zero-thickness interface separating the surface flow and the subsurface flow where the Darcy model applies. In that context, a particle tracking method for residence time calculation assumes that the release elevation (y_1) and exit elevation (y_2) of the tracked fluid parcels are both at the exact water-sediment interface. In the present DNS, there is a transition layer between the surface flow and the Darcy-flow region. This layer includes the roughness sublayer (Raupach et al., 1991)—a near-bed layer where form-induced stresses are important—and the Brinkman layer—the region of mean shear layer penetration, $\partial\langle\overline{u}\rangle/\partial y > 0$. Varying entry and exit elevations parcels are tested. Examples of tracked flow paths are sketched in Figure 2(a).

3 Results

3.1 Effect of bed roughness geometry on transit times

Figures 2(b) and 2(c) compare $\overleftarrow{P}_Q(\tau)$ and $\overleftarrow{p}_Q(\tau)$ with the same entry and exit elevations for two sets of values: $y_1 = y_2 = 0$ (near the sediment crest) and $y_1 = y_2 = -3D$ (a sufficiently deep elevation beyond which the median τ of the $\overleftarrow{p}_Q(\tau)$ distribution becomes largely independent of the entry and exit elevations for both cases, as shown later in Figure 5). The elevation $-3D$ is equivalent to -0.6δ. The transit times are normalized by the LETOT (δ/u_τ) of the open-channel turbulence, representative of the time scale of largest turbulent coherent motions in the water column. For large transit times stronger fluctuations of the TTD curves are seen in Figure 2(c), since the sampling of these long paths available from the DNS domain is extremely limited. The $\overleftarrow{p}_Q(\tau)$ distributions display power-law decays with a slope of around -1.3 at large transit times for both cases. The existence of a power-law tail indicates that the sediment domain in the DNS simulations is sufficiently large (in both x and y) to capture deeper flow paths, and is consistent with experimental observations by Aubeneau et al. (2015) and results of numerical simulations obtained by Lee et al. (2020) of exchanges induced by multi-scale bed geometries. Note that, according to Equation (5), a power-law decay of the TTD ($\overleftarrow{p}_Q$) is associated with a power-law decay of the RTD (p_S), which is shown in Figure S1 in the Supporting Information. For both cases, a deeper entry elevation excludes shorter flow paths close to the surface and, consequently, increases the probability of longer paths. This is reflected by the shifting of the TTDs toward larger times in Figure 2(c) as y_1 and y_2 change from 0 to $-3D$. The change of entry and exit elevations does not significantly modify the slope of the power-law tail.

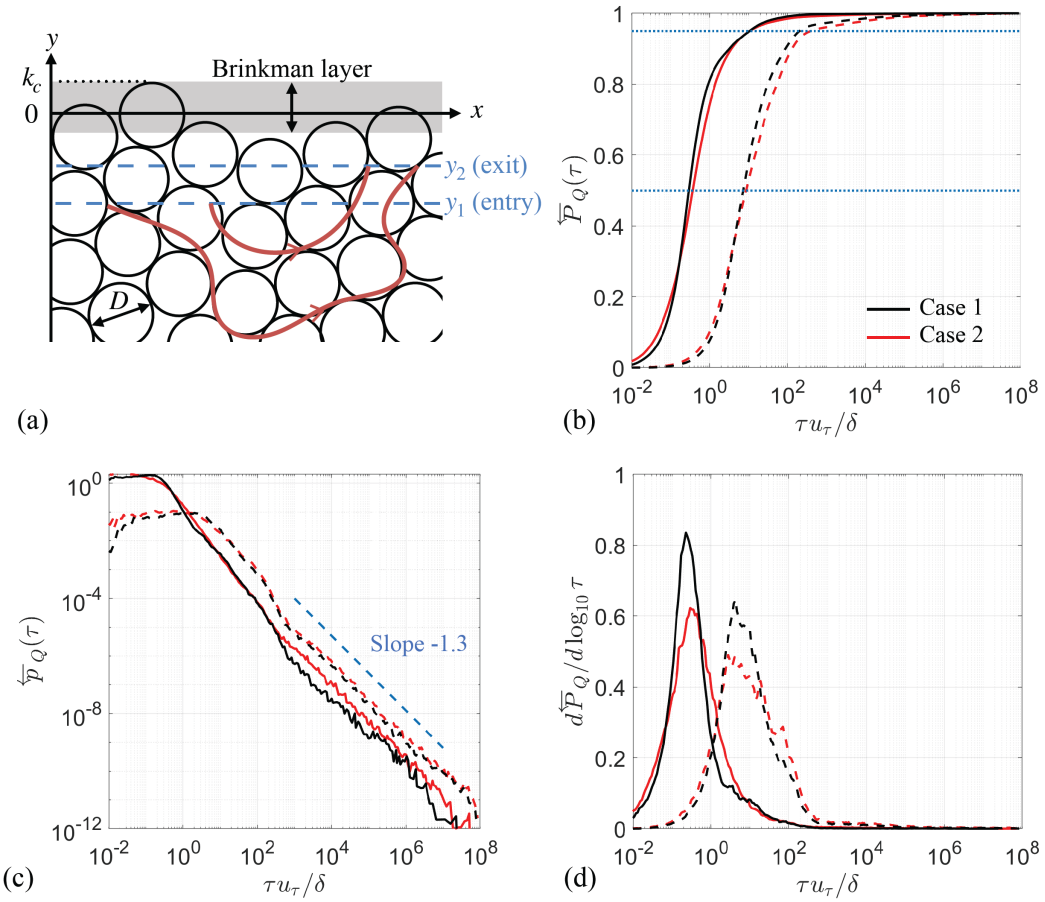

Figure 2. (a) Sketch of typical tracked flow paths for the random interface (Case 2). The cumulative backward transit time distribution (b) and its pdf (c) are shown for two sets of entry and exit locations: $y_1 = y_2 = 0$ (——) and $y_1 = y_2 = -3D$ (- - -) for the regular interface (black lines) and the random interface (red lines). (d) Modified pdf showing the probability density in evenly spaced logarithmic increments. In (b), the horizontal dashed lines (···) mark the 50th (median) and 95th percentiles. In (c), the dashed blue lines (- - -) show the fitted power law with slopes indicated.

Table 2. Various characteristics of transit times calculated based on mean advection only and both mean advection and molecular diffusion, at two elevations of particle entry (y_1) and exit (y_2). Transit times are normalized by δ/u_τ.

(y_1, y_2)	Characteristic	Case 1 (A)	Case 2 (A)	Case 1 (MD)	Case 2 (MD)
$(0, 0)$	τ_{50}	0.294	0.368	0.467	0.574
$(0, 0)$	τ_{95}	10.6	10.6	110	80.0
$(-3D, -3D)$	τ_{50}	7.33	8.67	13.6	13.8
$(-3D, -3D)$	τ_{95}	205	393	8.35×10^5	2.17×10^6

Note. 'A' denotes calculation based on time-mean advection alone; 'MD' denotes calculation accounting for both time-mean advection and molecular diffusion (discussed in Section 3.3).

When the particle release location at 0 was used, the $\overleftarrow{p}_Q$ distribution in the case with regular roughness displays a relatively sharp drop of probability for dimensionless τ at around 400. This is thought to be related to the organized fluid motions around the regularly arranged grains at the surface, leading to preferential values of τ associated with these short paths. A similar drop in probability is also evident at dimensionless τ of around 200 to 400 in both cases, when a particle release elevation of $-3D$ was used. This is because the algorithm tracks undulating segments of the large number of paths that reach not far beyond $y = -3D$ (visualized in Figures 3(e,f)). Lee et al. (2020) studied bed geometries synthesized with systematically varying spectral characteristics. They also observed variations in the slope of the RTD and suggested that they are connected to the flow recirculation regions induced by bed morphology.

An alternative approach to plot the transit time distribution, different from $\overleftarrow{p}_Q(\tau)$, is to divide the unit area under the curve into evenly spaced logarithmic increments of τ. This allows the actual probability density to be shown in a plot with a logarithmic τ axis. This distribution, shown in Figure 2(d), is defined as $d\overleftarrow{P}_Q/d\log_{10}\tau$ and is equivalent to $2.303\tau\overleftarrow{p}_Q$ (Grant et al., 2020).

To quantitatively compare the TTDs, the 50th and 95th percentiles (denoted as τ_{50} and τ_{95}, respectively) of the $\overleftarrow{p}_Q$ distributions are calculated. Specifically, τ_{50} represents the central tendency of the distribution, while τ_{95} is considered as a characteristic τ associated with the rare, long-transit-time subsurface paths. Their values are tabulated in Table 2 under columns "Case 1 (A)" and "Case 2 (A)". The comparison shows that the two cases give rather similar τ_{50} values (up to 10-20% different) for both elevations. For $y_1 = y_2 = -3D$, τ_{95} is significantly higher in Case 2 than in Case 1 (393 versus 205), due to longer and deeper reaching paths, which will be shown in Figure 3(g,h). An important conclusion that follows from this result is that the difference in bed roughness texture extends deep into the sediment and significantly modifies the transit time values.

To explain the differences in the TTD characteristics, Figure 3 shows tracked subsurface flow paths for $y_1 = y_2 = 0$ (a-d) and for $y_1 = y_2 = -3D$ (e-h) for both cases. Only the paths with travel times equal to τ_{50} and τ_{95} are plotted. In each subplot, around 200 pathlines are visualized. For both cases the paths associated with τ_{50} are short and do not reach beyond one grain diameter below y_1. Those associated with τ_{95}, however, reach far deeper and are described as follows. For the regular interface, relatively uniform small-scale arc-shaped paths are observed (due to flows around regularly packed grains at the bed surface). For the random case the tracked paths are more complex, with short paths near the interface and also longer, deeper paths. As the transit time of a water parcel depends on the depth and the length of the flow path, τ_{95} in Case 2 is longer

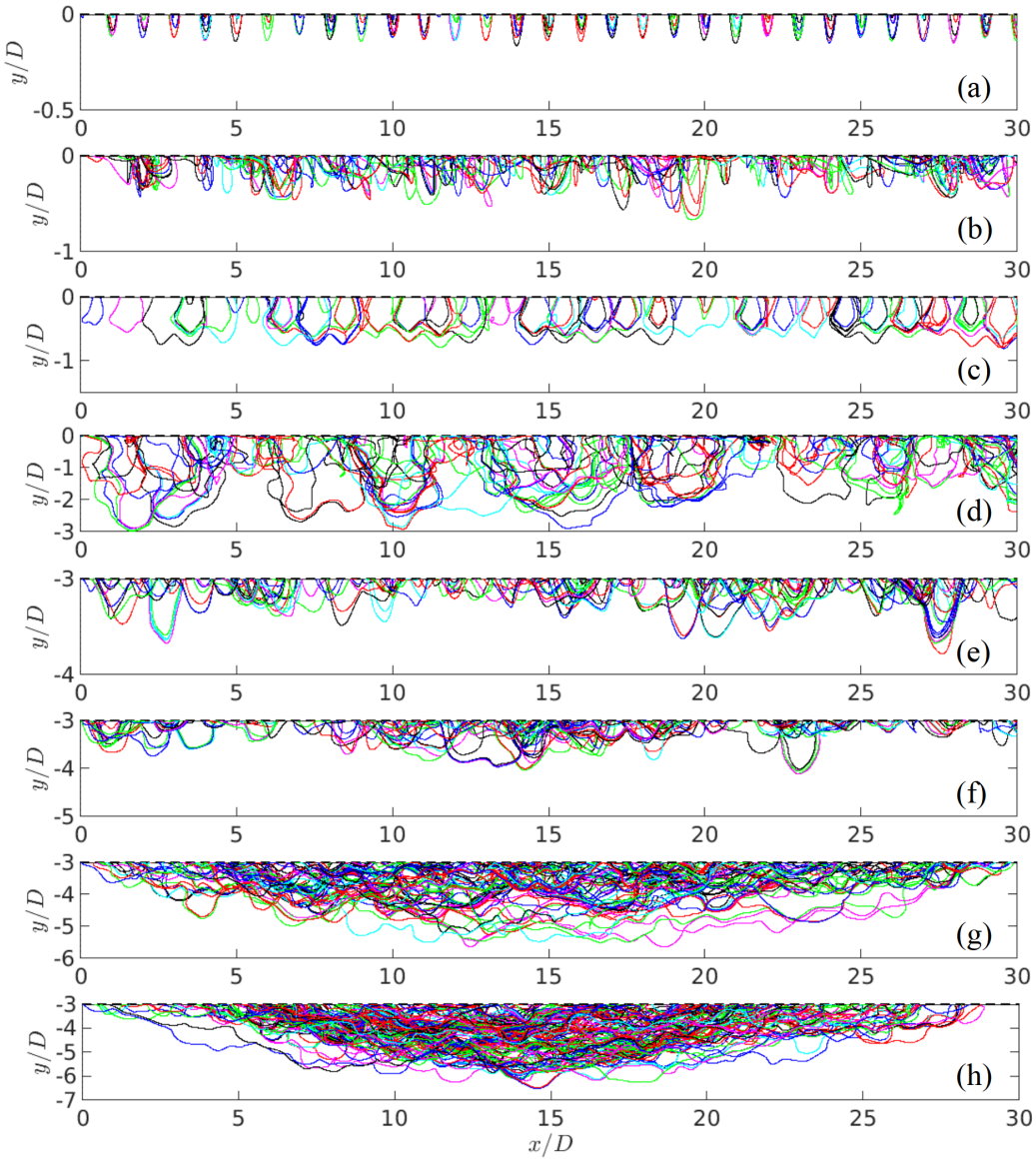

Figure 3. Time-mean subsurface flow paths corresponding to the median (50th-percentile) transit time (a,b,e,f) and the 95th-percentile transit time (c,d,g,h) for entry/exit elevations at $y_1 = y_2 = 0$ (a,b,c,d) and $y_1 = y_2 = -3D$ (e,f,g,h), for the regular (a,c,e,g) and random (b,d,f,h) interfaces.

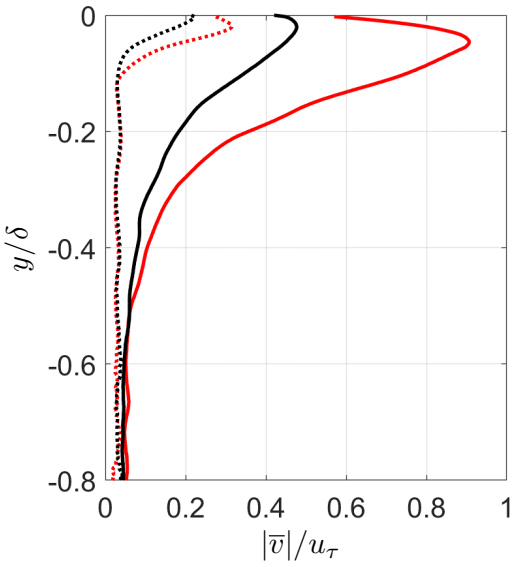

Figure 4. Wall-normal variation of $\overline{v}$ magnitude conditionally averaged along downward (red) or upward (black) flow paths tracked at $y_1 = y_2 = 0$, for regular (- - -) and random (———) cases.

than that in Case 1. For paths at $y_1 = y_2 = -3D$, Case 1 also yields multiscale flow paths similar to those for Case 2, as the short paths near the interface for Case 1 are now excluded by the deeper entry elevation. The paths in Case 2 reach deeper into the sediment than for Case 1, leading to longer transit times. These observations indicate that the flow pattern throughout the bed is dependent on the roughness characteristics.

In Figure 3, nearly all of the flow paths are oriented downstream in x. Exceptions are the flow paths located in the lower portion of the recirculation regions near the interface, where the flow is directed upstream. The very high fraction of subsurface flow paths oriented downstream is a major difference from flow paths induced by bedforms, such as those induced by triangular bedforms in the experimental study of Elliott and Brooks (1997a), where a significant fraction of large-scale upstream-oriented subsurface flow paths were found. This difference is probably due to the negligible hydrostatic pressure variations along the interface in the present cases as the roughness height is much lower than the open-channel height.

To characterize the velocity along the subsurface flow paths, Figure 4 compares the wall-normal velocity magnitudes ($|\overline{v}|$) that are conditionally averaged along the down- and up-going portions of the flow paths, respectively. The result is a function of y and the bed-normal flow path direction. Flow paths tracked with $y_1 = y_2 = 0$ are used. At a given y near the interface, $|\overline{v}|$ for the random case is much larger than the value for the regular case. This is consistent with the deeper flow paths for the former (Figure 3(d)) than for the latter (Figure 3(c)). In addition, for both cases the speed of downward flow is higher compared to that of upward flow. This difference has an impact on the transit time values when the entry elevation differs from the exit one.

Next, independent variations of entry (y_1) and exit (y_2) elevations are studied. Both y_1 and y_2 are varied between the sediment crest and $y/\delta = -0.9$. An ensemble of particle-tracking simulations based on 42 values each of y_1 and y_2 (total 1764) was carried out. For each (y_1, y_2) pair, τ_{50} is calculated and plotted in a map shown in Figure 5. The vari-

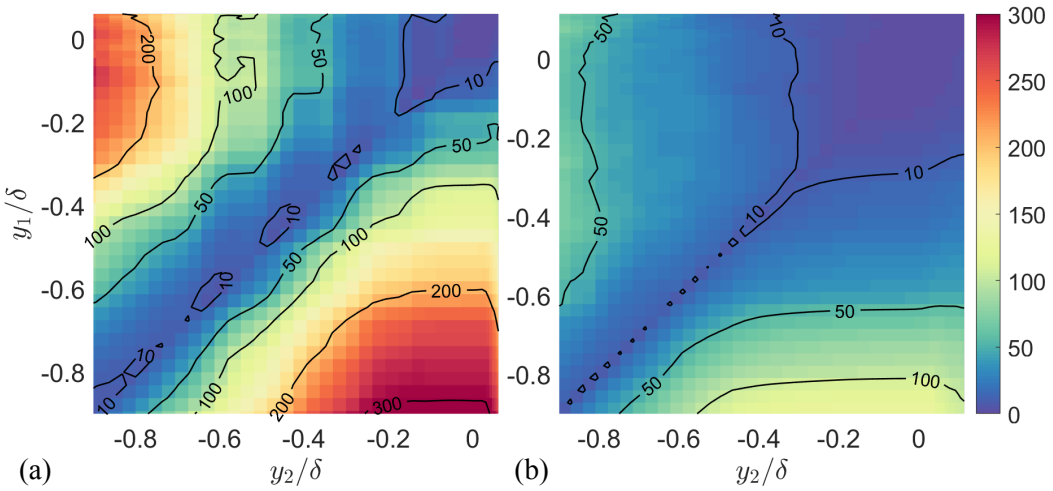

Figure 5. Median transit time normalized by δ/u_τ with independent variations of y_1 (entry) and y_2 (exit) elevations, for regular (a) and random (b) cases. Similar variations of τ_{95} are shown in the Supporting Information Figure S5.

ation of τ_{95} was also evaluated and a similar comparison was observed; the τ_{95} plots are shown in the Supporting Information Figure S5.

First, focus on the diagonal line represented by $y_1 = y_2$. The short transit times of $o(1)\delta/u_\tau$ at $y_1 = y_2 \approx 0$ are mostly due to mild undulations of subsurface paths (Figure 3a,b). For sufficiently deep entry/exit elevations, τ_{50} plateaus to values of $o(10)\delta/u_\tau$. The dependence of transit times on the entry and exit elevations of particles is not restricted to elevation variation within the Brinkman layer, which corresponds approximately to $y/\delta \in (-0.1, 0.1)$. Beyond this layer, deeper entry or exit elevations will still result in progressively longer transit times due to progressive exclusion of shorter flow paths, until only long flow paths remain.

Next, small values of $|y_1 - y_2|$ produce short transit times due to a large fraction of tracked paths being associated with short flow paths that do not extend far beyond the elevation of y_1, while with large $|y_1 - y_2|$ differences a larger fraction of the tracked paths are longer and deep-reaching ones, which yields much longer transit times. The regions above the diagonal line (i.e., $y_1 > y_2$) and below the line (i.e., $y_1 < y_2$) are not symmetric. The median transit times with y_1 below y_2 are larger than those with y_1 above y_2 at the same $|y_1 - y_2|$ difference. This is because the downward motion of a fluid parcel in the bed is, on average, faster than the upward motion, as shown in Figure 4. One also observes that the median transit times with $y_1 > y_2$ are less well-converged statistically than those with $y_1 < y_2$, as shown by the more fluctuating contour lines. This is due to the fewer flow paths used for averaging when $y_1 > y_2$ in the current computation procedure (see Supporting Information, Section S3 and Figure S3). At large y_1-y_2 separations, much longer transit times are observed for the regular case compared to the random one. This difference is probably a result of the significantly smaller magnitude of bed-normal velocity along flow paths in the regular case for $y/\delta > -0.5$ (Figure 4).

These results highlight the fact that subsurface flow paths are multiscale in nature and typically extend deeper beyond the Brinkman layer. They also show that both the entry and exit elevations are important parameters in measuring and reporting transit times in the presence of bed roughness; however, these details are not often presented

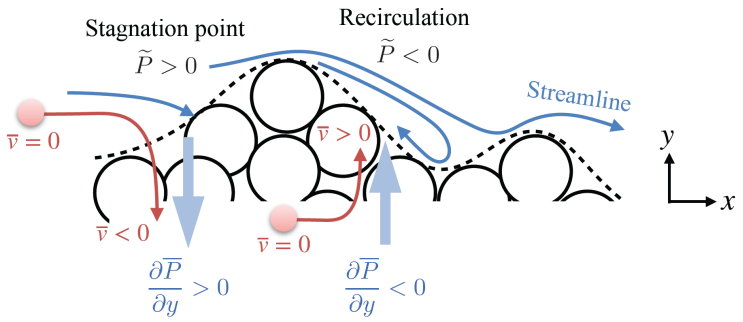

Figure 6. Sketch showing how local high-pressure (stagnation point) and low-pressure (recirculation) regions lead to entry and exit of fluid parcels (red spheres and red lines), specifically, in Case 2. **---** Roughness geometry. $\overline{P}(x,y,z)$ and $\overline{v}(x,y,z)$ are the time-averaged values of pressure and wall-normal velocity; $\widetilde{P}(x,y,z) = \overline{P}(x,y,z) - \langle\overline{P}\rangle(y)$ is the form-induced pressure, i.e., deviations from the plane-averaged value.

in the literature. The roughness geometry affects not only the transit time when y_1 is set equal to y_2, but also the dependence of transit time on y_1 and y_2 when $y_1 \neq y_2$.

In the next two sections we address the following questions: (1) What factors determine the (x,z) locations of the entries and exits of subsurface flow paths (and consequently TTD characteristics)? (2) How important is the molecular diffusion for solute transit time?

3.2 Interfacial $\overline{v}$ distribution

Figure 6 shows the typical flow pattern around a roughness protuberance formed as a grain cluster. A stagnation point appears upstream of the protuberance, leading to a region with local $\overline{P}$ higher than the spatial average (indicated by $\widetilde{P} > 0$). In addition, a recirculation region appears downstream, leading to a local low-$\overline{P}$ region (indicated by $\widetilde{P} < 0$). Such interfacial pressure variation is in line with the description of local pressure variation on a bedform (triangular dune) by Savant et al. (1987). These local pressure maxima and minima lead to bed-normal pressure gradients at the bed surface: $\partial\overline{P}/\partial y > 0$ upstream and $\partial\overline{P}/\partial y < 0$ downstream.

The bed-normal mean momentum equation near the interface connects the pressure gradients to the entry and exit of subsurface flow paths:

$$\frac{\overline{D}\overline{v}}{\overline{D}t} \equiv \frac{\partial\overline{v}}{\partial t} + \overline{u}_i\frac{\partial\overline{v}}{\partial x_i} = -\frac{1}{\rho}\frac{\partial\overline{P}}{\partial y} - \frac{\partial\overline{u_i'v'}}{\partial x_i} + \nu\frac{\partial^2\overline{v}}{\partial x_i\partial x_i}, \tag{7}$$

where $\overline{D}\overline{v}/\overline{D}t$ is the material derivative of $\overline{v}$ advected by the time-mean flow, and the three terms on the right-hand-side represent forces due to, respectively, time-mean pressure, Reynolds stress and viscous stress. Equation (7) describes how various factors (on the right-hand-side) affect the time-mean v velocity of a fluid parcel. It is hypothesized that the local pressure gradient (the first term on the right-hand-side of (7)) is the main factor in determining the entry ($\overline{v} < 0$) and exit ($\overline{v} > 0$) locations of subsurface flow paths. Specifically, a positive $\partial\overline{P}/\partial y$ upstream of the obstacle would lead to negative $\overline{v}$ values (entries of flow paths) for a fluid parcel initially with $\overline{v} = 0$, while a negative $\partial\overline{P}/\partial y$ downstream would lead to exits of flow paths. Such mechanism is sketched in Figure 6. This hypothesis is to be validated next.

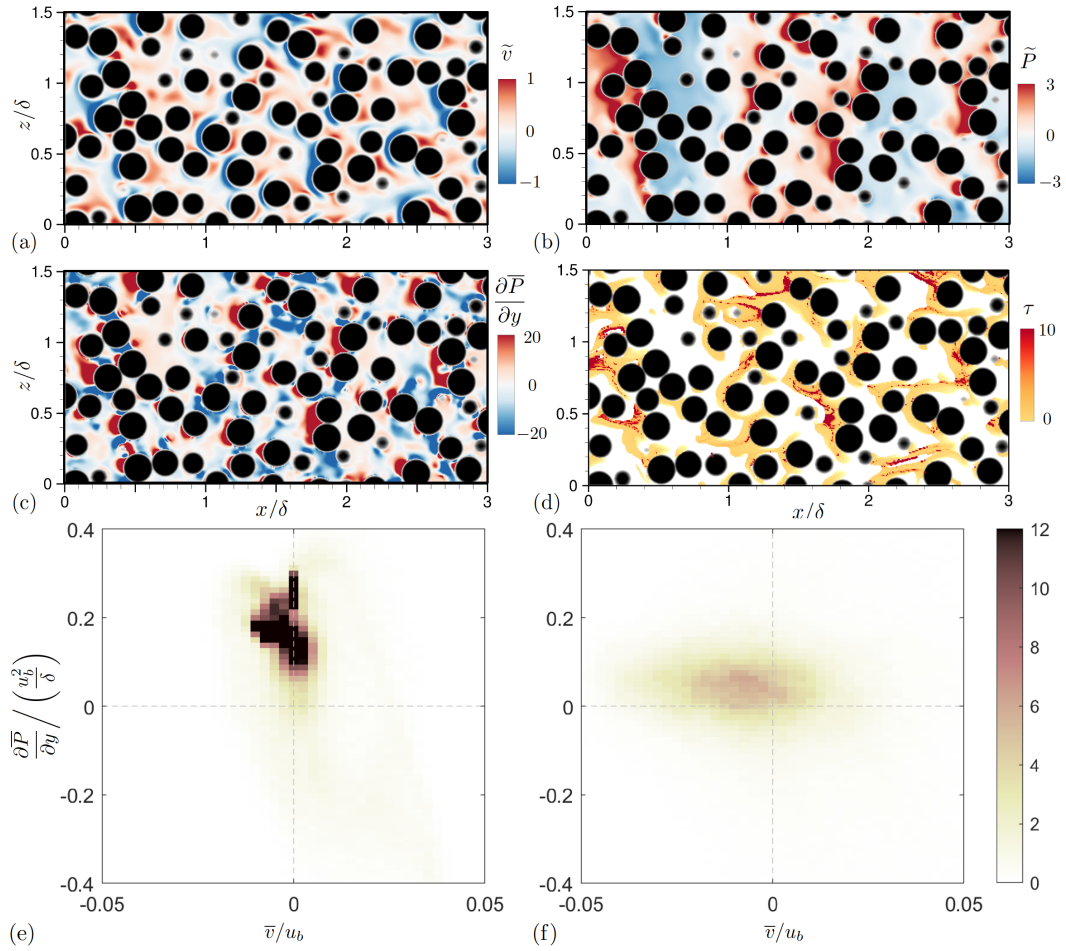

Figure 7. Bed-parallel contours for the random interface (Case 2) at $y = 0$: (a) bed-normal mean velocity, (b) form-induced pressure, (c) bed-normal gradient of mean pressure, and (d) transit time of flow paths entering at each location. Only 1/4 of the domain is shown. All quantities in (a-d) are normalized by δ and u_τ. Joint probability density functions of $\partial\overline{P}/\partial y$ and $\overline{v}$ in the interface region, for Case 1 (e) and Case 2 (f).

Figures 7(a-d) compare contours of $\overline{v}$, $\widetilde{P}$, and $\partial\overline{P}/\partial y$ in a bed-parallel plane at $y = 0$ for the random case. The correlation between positive-$\widetilde{P}$ regions, positive y-gradients of pressure, and negative $\overline{v}$ values (entries), is apparent. These regions are typically seen upstream of clusters of grains serving as roughness protuberances. Similarly, downstream of these protuberances, one typically observes low pressure values, negative pressure gradients, and positive $\overline{v}$ (exits). Figure 7(d) shows the contour of transit time of flow paths entering the subsurface from this plane. Regions with the highest pressure values are seen to generate the longest transit times.

The local correlation between $\overline{v}$ and the bed-normal pressure gradients is better demonstrated using contours of their joint probability density function (jpdf) in Figures 7(e,f) for the two cases, respectively. Since the local y-gradient of $\overline{P}$ varies significantly in y between the crest elevation and the bottom of the Brinkman layer, here the jpdf value for each $\partial\overline{P}/\partial y$ and $\overline{v}$ combination is calculated at every y grid point in the region bounded by these two elevations and then averaged. The jpdf values shown in Figure 7(e,f) are normalized such that the area integral in each of these two plots is one. Both quantities are normalized by δ and the bulk velocity (u_b) in the water column; u_b is calculated as $1/\delta \int_0^\delta \langle\overline{u}\rangle dy$. Here u_b instead of u_τ is used for normalization to highlight the effect of roughness geometry. For both cases, the vertical pressure gradients are indeed negatively correlated with the vertical flux. Comparing the two cases, the random case displays much wider distribution of $\overline{v}$ and narrower distribution of y-gradient of pressure. This means that $\overline{v}$ is more sensitive in this case to changes in $\partial\overline{P}/\partial y$, probably because of the higher effective permeability near the interface than for the regular case (Shen et al., 2020). Notice also that in both cases the magnitude of $\overline{v} < 0$ reaches much higher values than the magnitude of $\overline{v} > 0$, again indicating faster fluid parcel entry into the bed than exit from the bed.

Figure 7 indicates that, for both cases, the interfacial pressure distribution is closely correlated with local $\overline{v}$ and therefore is probably the driving force of $\overline{v}$ transport near the interface. Forces of the Reynolds and viscous stresses play secondary roles. In other words, the differences in transit time characteristics between Cases 1 and 2 are probably due to the different interfacial pressure distributions caused by the roughness geometries obstructing the surface flow in different ways.

3.3 Effect of molecular diffusion on TTD

The transit time calculation using Equation (6) considers the movement of a fluid parcel. On the other hand, the transit time of a solute is affected also by molecular diffusion. An exact estimation of the solute transit time would require tracking either the instantaneous location of a tracer particle (during the DNS simulation) or the concentration variation which yields a breakthrough curve. These tasks are beyond the scope of the present work. An alternative approach is to use the random walk method (Kinzelbach, 1988) to incorporate the effect of molecular diffusion into Equation (6) and this approach is used here.

The random walk particle tracking is based on a set of stochastic differential equations. Following Sun et al. (2015) who carried out pore-scale random walk particle tracking for a 3D domain, we solve

$$x_i(t + \Delta t) = x_i(t) + \overline{u}_i(x_i, t)\Delta t + r_i\sqrt{2D_m\Delta t}, \tag{8}$$

where Δt is a small time differential, r_i is a random number of standard Gaussian distribution with unit variance and zero mean, and D_m is the molecular diffusion coefficient. Equation (8) is a generalization of Equation (6). Compared to the approach of Kinzelbach (1988), here the dispersion terms are ignored by setting the longitudinal and transverse dispersivity lengths to zeros. This is because the DNS resolves the time-mean flow details. Note also that the diffusion due to the turbulent velocities u_i' is assumed to be much

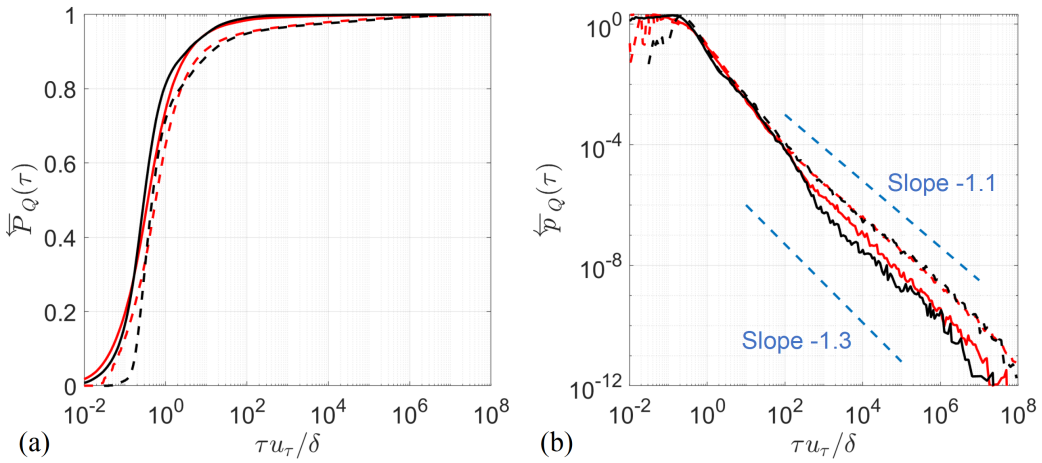

Figure 8. Cumulative backward transit time distribution (a) and its pdf (b) based on mean advection only (———) and based on both mean advection and molecular diffusion (- - -), for Case 1 (black) and Case 2 (red) at $y_1 = y_2 = 0$. In (b), - - - shows the fitted power law with slope indicated.

smaller than that due to $\widetilde{u}_i$ because of much weaker Reynolds stresses compared to the dispersive stresses below the interface. The smoothness of the results of Equation (8) requires the step of particle advection to be a fraction of the grid cell size; Kinzelbach (1988) recommended five to ten steps per cell. Here, the Δt value corresponds to five steps per grid cell at a convection velocity of $\langle\overline{u}\rangle$ below the Brinkman layer. $D_m/u_\tau\delta$ takes a value of 2.5×10^{-6} to achieve a Schmidt number ($Sc = \nu/D_m$) of around 1000, representative of dissolved oxygen in water.

The backward TTD and its cumulative distribution are shown in Figure 8 for $y_1 = y_2 = 0$. Various TTD characteristics are tabulated in Table 2 under columns "Case 1 (MD)" and "Case 2 (MD)". The TTD power-law decay slope is milder for both cases, with the slope of around -1.1, compared to -1.3 considering advection only. Changing to a deeper elevation, such as $y_1 = y_2 = -3D$, does not affect the power-law slope. For both cases, the addition of molecular diffusion increases significantly the probability of transit times being longer than $o(10^2)\delta/u_\tau$, while early time values are only slightly affected. This increase in transit times is attributed to the fact that solute particles are displaced from the time-mean paths by molecular diffusion, resulting in paths with greater lengths. The addition of molecular diffusion does not remove the difference brought by a change in the roughness geometry. For a particle release elevation below the interface region (i.e. $y_1 = y_2 = -3D$) which tracks a large fraction of deep subsurface paths, τ_{95} normalized by δ/u_τ is significantly longer in Case 2 (2.17×10^6) than in Case 1 (8.35×10^5).

For a 2D sinusoidal bedform analyzed using an advection-dispersion model, Bottacin-Busolin and Marion (2010) also observed a milder slope (-0.5) of the residence time function when both mean advection and mechanical dispersion were accounted for, compared to the slope with advection only (-1.0). According to Equation (5) and the Supporting Information Section S1, the present slopes of $\overleftarrow{P}_Q$ shown in Figure 8(b) indicate power-law decay slopes of -0.1 and -0.3 of the same residence time function, with or without molecular diffusion, respectively. The difference between the slopes observed herein and those in the study of Bottacin-Busolin and Marion (2010) is possibly due to the three-

dimensionality of the present flow and the capability of DNS in capturing the actual velocities near the interface and within the bed.

4 Conclusions

Results of transit times are reported for turbulent open-channel flows over flat sediment beds at $Re_\tau = 395$ and $Re_K = 2.6$, with two different bed roughnesses consisting of either regularly (Case 1) or randomly (Case 2) positioned sediment grains at the bed surface. The transit time calculations are based on DNS simulations similar to the ones reported in Shen et al. (2020). The transit times are calculated using the particle tracking method, considering (i) advection by time-mean velocity only and (ii) both time-mean advection and molecular diffusion.

Despite the absence of bedforms, both bed roughnesses generated a large spectrum of transit times, whose characteristics are similar to those generated by bedforms. The TTDs show power-law tails at late times for both cases; the time range and slope of the tail vary only weakly with the roughness geometry. For both cases, the power-law slopes range from -1.3 considering the mean advection only, and around -1.1 considering both the mean advection and the molecular diffusion. We also show that, with pore-resolved data, the definition of a surface-subsurface interface becomes obscure; the calculated transit times vary with the elevations chosen to mark the 'entry' or 'exit' of particles.

Near the interface, roughness leads to regions with local pressure maxima or minima due to its effect on the near-bed turbulence. These regions are found to correlate closely with the distribution of interfacial bed-normal velocity. This suggests that locations of subsurface flow path entries and exits are mainly determined by the interfacial pressure, while being less sensitive to forces due to the Reynolds and viscous stresses. In other words, the advective pumping mechanism may be used to describe the subsurface flow induced by roughness on a macroscopically flat bed, similar to those induced by bedforms.

Compared to the regular roughness, the random roughness leads to longer transit times in the TTD power-law tail associated with deep subsurface pathlines. Specifically, the pure-advection particle tracking in Case 2 yields 18% and 91% larger transit times of the 50th and the 95th percentiles, respectively, than in Case 1 when $y_1 = y_2 = -3D$. This difference occurs because the random roughness induces more intense interfacial pressure variation (due to grain clusters forming protuberances larger than a single grain), with a wider range of horizontal length scales. Consequently, the subsurface flow paths in Case 2 can reach farther and deeper than in Case 1. With the addition of molecular diffusion in the transit time calculation, the transit time increases (especially at late times) for both cases, as expected. The differences between the two cases remain significant.

This work demonstrates that grain-scale roughness and its geometry are important for hyporheic exchange, as shown by the subsurface flow characteristics and transit times. The effect appears to be fundamentally similar to how a larger-scale bedform affects the exchange. These findings would not have been possible if a pore-unresolved simulation model (such as the Darcy flow model) was used instead. In addition, DNS data similar to the present data can be used for closure developments, such as the parameterization of advection due to $\widetilde{u}_i$ and u_i' in TTD or RTD prediction based on a Darcy flow. Additional factors that are likely to affect the overall transit time of solutes include (i) grain-scale solute concentration variation near the bed surface and (ii) turbulent diffusion, which is strong in the Brinkman layer and is likely to affect τ values calculated with y_1 or y_2 close to 0. The importance of these factors and their dependence on roughness details need to be addressed in future work. In addition, scenarios that include both roughness and bedforms need to be explored for possible interactions between the effects of the two.

Conflict of Interest

Authors declare no conflicts of interest.

Data Availability Statement

Flow field data, sediment geometries, tracked subsurface flow paths, and transit time data are publicly available (Shen et al., 2022) at https://doi.org/10.5281/zenodo.5895145.

Acknowledgements

The authors thank Professor Stanley Grant, two anonymous reviewers, and the Associate Editor for their helpful review of the manuscript. This work was supported in part through computational resources and services provided by the Institute for Cyber-Enabled Research at Michigan State University.

References

Aubeneau, A. F., Martin, R. L., Bolster, D., Schumer, R., Jerolmack, D., & Packman, A. (2015). Fractal patterns in riverbed morphology produce fractal scaling of water storage times. *Geophysical Research Letters*, *42*(13), 5309–5315.

Baranov, V., Lewandowski, J., & Krause, S. (2016). Bioturbation enhances the aerobic respiration of lake sediments in warming lakes. *Biology Letters*, *12*, 20160448.

Battin, T. J., Kaplan, L. A., Findlay, S., Hopkinson, C. S., Marti, E., Packman, A. I., ... Sabater, F. (2008). Biophysical controls on organic carbon fluxes in fluvial networks. *Nature Geoscience*, *1*, 95–100.

Benettin, P., Kirchner, J. W., Rinaldo, A., & Botter, G. (2015). Modeling chloride transport using travel time distributions at Plynlimon, Wales. *Water Resources Research*, *51*(5), 3259–3276.

Benettin, P., Rinaldo, A., & Botter, G. (2013). Kinematics of age mixing in advection-dispersion models. *Water Resources Research*, *49*(12), 8539–8551.

Boano, F., Harvey, J. W., Marion, A., Packman, A. I., Revelli, R., Ridolfi, L., & Wörman, A. (2014). Hyporheic flow and transport processes: Mechanisms, models, and biogeochemical implications. *Reviews of Geophysics*, *52*(4), 603–679.

Bottacin-Busolin, A., & Marion, A. (2010). Combined role of advective pumping and mechanical dispersion on time scales of bed form-induced hyporheic exchange. *Water Resources Research*, *46*(8).

Botter, G., Bertuzzo, E., & Rinaldo, A. (2011). Catchment residence and travel time distributions: The master equation. *Geophys. Res. Lett.*, *38*, L11403-1—6.

Breugem, W. P., Boersma, B., & Uittenbogaard, R. E. (2006). The influence of wall permeability on turbulent channel flow. *J. Fluid Mech.*, *562*, 35–72.

Chandler, I. D., Guymer, I., Pearson, J. M., & van Egmond, R. (2016). Vertical variation of mixing within porous sediment beds below turbulent flows. *Water Resour. Res.*, *52*, 3493–3509.

Dairain, A., Maire, O., Meynard, G., Richard, A., Rodolfo-Damiano, T., & Orvain, F. (2020). Sediment stability: can we disentangle the effect of bioturbating species on sediment erodibility from their impact on sediment roughness? *Marine Environmental Research*, *162*, 105147.

Danesh-Yazdi, M., Foufoula-Georgiou, E., Karwan, D. L., & Botter, G. (2016). Inferring changes in water cycle dynamics of intensively managed landscapes via the theory of time-variant travel time distributions. *Water Resources Research*, *52*(10), 7593–7614.

Dey, S., & Das, R. (2012). Gravel-bed hydrodynamics: double-averaging approach. *Journal of Hydraulic Engineering*, *138*(8), 707–725.

Elliott, A. (1991). Transfer of solutes into and out of streambeds. *Ph. D. Dissertation, California Institute of Technology*.

Elliott, A., & Brooks, N. (1997a). Transfer of nonsorbing solutes to a streambed with bed forms: Laboratory experiments. *Water Resources Research*, *33*(1), 137–151.

Elliott, A., & Brooks, N. (1997b). Transfer of nonsorbing solutes to a streambed with bed forms: Theory. *Water Resources Research*, *33*(1), 123–136.

Fang, H., Han, X., He, G., & Dey, S. (2018). Influence of permeable beds on hydraulically macro-rough flow. *Journal of Fluid Mechanics*, *847*, 552–590.

Flack, K. A., & Schultz, M. P. (2014). Roughness effects on wall-bounded turbulent flows. *Phys. Fluids*, *26*, 101305.

Grant, S. B., Gomez-Velez, J. D., Ghisalberti, M., Guymer, I., Boano, F., Roche, K. R., & Harvey, J. (2019). A one-dimensional model for turbulent mixing in the benthic biolayer of stream and coastal sediments. *Water Resour. Res.*, *56*, e2019WR026822.

Grant, S. B., Monofy, A., Boano, F., Gomez-Velez, J. D., Guymer, I., Harvey, J., & Ghisalberti, M. (2020). Unifying advective and diffusive descriptions of bedform pumping in the benthic biolayer of streams. *Water Resour. Res.*, *56*, e2020WR027967.

Han, X., Fang, H., He, G., & Reible, D. (2018). Effects of roughness and permeability on solute transfer at the sediment water interface. *Water Research*, *129*, 39–50.

Harman, C. J. (2015). Time-variable transit time distributions and transport: Theory and application to storage-dependent transport of chloride in a watershed. *Water Resour. Res.*, *51*, 1–30.

Harvey, J. W., Böhlke, J. K., Voytek, M. A., Scott, D., & Tobias, C. R. (2013). Hyporheic zone denitrification: Controls on effective reaction depth and contribution to whole-stream mass balance. *Water Resources Research*, *49*(10), 6298–6316.

Harvey, J. W., Bohlke, J. K., Voytek, M. A., Scott, D., & Tobias, C. R. (2013). Hyporheic zone denitrification: Controls on effective reaction depth and contribution to whole-stream mass balance. *Water Resour. Res.*, *49*, 6298–6316.

Jiménez, J. (2004). Turbulent flows over rough walls. *Annu. Rev. Fluid Mech.*, *36*, 173–196.

Keating, A., Piomelli, U., Bremhorst, K., & Nesic, S. (2004). Large-eddy simulation of heat transfer downstream of a backward-facing step. *Journal of Turbulence*, *5*(20), 1–3.

Kim, Blois, G., Best, J., & Christensen, K. (2020). Experimental evidence of amplitude modulation in permeable-wall turbulence. *J. Fluid Mech.*, *887*.

Kim, & Kang, P. (2020). Anomalous transport through free-flow-porous media interface: Pore-scale simulation and predictive modeling. *Advances in Water Resources*, *135*, 103467.

Kinzelbach, W. (1988). The random walk method in pollutant transport simulation. In *Groundwater flow and quality modelling* (pp. 227–245). Springer.

Knapp, J. L. A., Gonzalez-Pinzon, R., Drummond, J. D., Larsen, L. G., Cirpka, O. A., & Harvey, J. W. (2017). Tracer-based characterization of hyporheic exchange and benthic biolayers in streams. *Water Resour. Res.*, *53*, 1575–1594. doi: 10.1002/2016WR019393

Laube, G., Schmidt, C., & Fleckenstein, J. (2018). The systematic effect of streambed conductivity heterogeneity on hyporheic flux and residence time. *Adv. Water Resour.*, *122*, 60–69.

Lee, A., Aubeneau, A. F., & Cardenas, M. B. (2020). The sensitivity of hyporheic exchange to fractal properties of riverbeds. *Water Resour. Res.*,

56, e2019WR026560-1–15.

Malard, F., Tockner, K., Dole-Oliver, M. J., & Ward, J. (2002). A landscape perspective of surface–subsurface hydrological exchanges in river corridors. *Freshwater Biology*, *47*(4), 621–640.

Manes, C., Poggi, D., & Ridolfi, L. (2011). Turbulent boundary layers over permeable walls: scaling and near-wall structure. *J. Fluid Mech.*, *687*, 141–170.

Manes, C., Pokrajac, D., McEwan, I., & Nikora, V. (2009). Turbulence structure of open channel flows over permeable and impermeable beds: A comparative study. *Physics of Fluids*, *21*(12), 125109.

Mangavelli, S. C., Yuan, J., & Brereton, G. J. (2021). Effects of surface roughness topography in transient channel flows. *J. Turbul.*, *22*, 434–460.

Packman, A. I., Brooks, N. H., & Morgan, J. J. (2000). A physicochemical model for colloid exchange between a stream and a sand streambed with bed forms. *Water Resources Research*, *36*(8), 2351–2361.

Persson, N. J., Albohr, O., Tartaglino, U., Volokitin, A. I., & Tosatti, E. (2005). On the nature of surface roughness with application to contact mechanics, sealing, rubber friction and adhesion. *J. Phys.: Condens. Matter*, *17*, R1–R62.

Piomelli, U., & Yuan, J. (2013). Numerical simulations of spatially developing, accelerating boundary layers. *Phys. Fluids*, *25*, 101304-1—21.

Plimpton, S. (1995). Fast parallel algorithms for short-range molecular dynamics. *Journal of Computational Physics*, *117*(1), 1–19.

Raupach, M. R., Antonia, R. A., & Rajagopalan, S. (1991). Rough-wall boundary layers. *Appl. Mech. Rev.*, *44*, 1–25.

Raupach, M. R., & Shaw, R. (1982). Averaging procedures for flow within vegetation canopies. *Boundary-Layer Meteorology*, *22*(1), 79–90.

Roche, K. R., Li, A., Bolster, D., Wagner, G. J., & Packman, A. I. (2019). Effects of turbulent hyporheic mixing on reach-scale transport. *Water Resources Research*, *55*(5), 3780–3795.

Salehin, M., Packman, A. I., & Paradis, M. (2004). Hyporheic exchange with heterogeneous streambeds: Laboratory experiments and modeling. *Water Resources Research*, *40*(11).

Savant, A. S., Reible, D. O., & Thibodeaux, L. (1987). Convective transport within stable river sediments. *Water Resour. Res.*, *23*, 1763–1768.

Scotti, A. (2006). Direct numerical simulation of turbulent channel flows with boundary roughened with virtual sandpaper. *Physics of Fluids*, *18*(3), 031701.

Shen, G., Yuan, J., & Phanikumar, M. S. (2020). Direct numerical simulations of turbulence and hyporheic mixing near sediment–water interfaces. *Journal of Fluid Mechanics*, *892*, A20. doi: 10.1017/jfm.2020.173

Shen, G., Yuan, J., & Phanikumar, M. S. (2022, January). *Dataset for "Quantifying the effects of bed roughness on transit time distributions via direct numerical simulations of turbulent hyporheic exchange".* Zenodo. doi: 10.5281/zenodo.5895145

Song, X., Chen, X., Zachara, J. M., Gomez-Velez, J. D., Shuai, P., Ren, H., & Hammond, G. E. (2020). River dynamics control transit time distributions and biogeochemical reactions in a dam-regulated river corridor. *Water Resources Research*, *56*(9), e2019WR026470.

Stubbs, A., Stoesser, T., & Bockelmann-Evans, B. (2018). Developing an approximation of a natural, rough gravel riverbed both physically and numerically. *Geosciences*, *8*, 449.

Sun, Y., Park, C.-H., Pichot, G., & Taron, J. (2015). Random walk particle tracking. In *Thermo-hydro-mechanical-chemical processes in fractured porous media: Modelling and benchmarking* (pp. 153–184). Springer.

Voermans, J., Ghisalberti, M., & Ivey, G. (2017). The variation of flow and turbulence across the sediment-water interface. *Journal of Fluid Mechanics*, *824*, 413–437.

Voermans, J., Ghisalberti, M., & Ivey, G. (2018). A model for mass transport across the sediment-water interface. *Water Resour. Res.*, *54*, 2799–2812.

Wörman, A., Packman, A. I., Johansson, H., & Jonsson, K. (2002). Effect of flow-induced exchange in hyporheic zones on longitudinal transport of solutes in streams and rivers. *Water Resources Research*, *38*(1), 2–1.

Worman, A., Packman, A. I., Marklund, L., & Harvey, J. W. (2006). Exact three-dimensional spectral solution to surface-groundwater interactions with arbitrary surface topography. *Geophys. Res. Lett.*, *33*, L07402.

Wu, W., Piomelli, U., & Yuan, J. (2019). Turbulence statistics in rotating channel flows with rough walls. *Int. J. Heat Fluid Flow*, *80*, 108467-1–13.

Yuan, J., Mishra, A. A., Brereton, G. J., Iaccarino, G., & Vartdal, M. (2019). Single-point structure tensors in turbulent channel flows with smooth and wavy walls. *Phys. Fluids*, *31*, 125115-1–15.

Yuan, J., & Piomelli, U. (2014a). Numerical simulations of sink-flow boundary layers over rough surfaces. *Physics of Fluids*, *26*(1), 015113.

Yuan, J., & Piomelli, U. (2014b). Roughness effects on the Reynolds stress budgets in near-wall turbulence. *Journal of Fluid Mechanics*, *760*.